Molecular Donor–Acceptor Dyads for Efficient Single-Material Organic Solar Cells

Sebastian Lucas, Jochen Kammerer, Martin Pfannmöller, Rasmus R. Schröder, Yakun He, Ning Li, Christoph J. Brabec, Tim Leydecker, Paolo Samorì, Tomasz Marszalek, Wojchiech Pisula, Elena Mena-Osteritz, and Peter Bäuerle*

Dedicated to Professor Franz Effenberger on the occasion of his 90th birthday

Single-material organic solar cells (SMOSCs) promise several advantages with respect to prospective applications in printed large-area solar foils. Only one photoactive material has to be processed and the impressive thermal and photochemical long-term stability of the devices is achieved. Herein, a novel structural design of oligomeric donor–acceptor (D–A) dyads 1–3 is established, in which an oligothiophene donor and fullerene acceptor are covalently linked by a flexible spacer of variable length. Favorable optoelectronic, charge transport, and self-organization properties of the D–A dyads are the basis for reaching power conversion efficiencies up to 4.26% in SMOSCs. The dependence of photovoltaic and charge transport parameters in these ambipolar semiconductors on the specific molecular structure is investigated before and after post-treatment by solvent vapor annealing. The inner nanomorphology of the photoactive films of the dyads is analyzed with transmission electron microscopy (TEM) and grazing-incidence wide-angle X-ray scattering (GIWAXS). Combined theoretical calculations result in a lamellar supramolecular order of the dyads with a D–A phase separation smaller than 2 nm. The molecular design and the precise distance between donor and acceptor moieties ensure the fundamental physical processes operative in organic solar cells and provide stabilization of D–A interfaces.

1. Introduction

Covalently linked donor–acceptor (D–A) dyads, triads, and multiads have been extensively investigated in the context of photoinduced energy and charge transfer (CT) processes, which are fundamental for natural photosynthesis, but as well important for the function of organic solar cells.[1,2] The nature and length of the molecular spacer bridging D and A, flexible nonconjugated or rod-like conjugated, polar or nonpolar, play an important role for the various fundamental processes such as excitation and energy transfer, CT, charge separation, and recombination.[3] CT is also dependent on the environment,[4] which severely comes into play for the photoinduced elementary processes of molecular D–A systems in the solid state, a scenario, encountered in organic electronic devices. In this respect, in thin films, aggregation of the molecules into supramolecular assemblies to form photoactive nanostructures with well-segregated A and D domains and their orientation relative to the substrate play a major role for efficient organic solar cells.[5] As a consequence, the tailoring of molecular properties in D–A systems is an important aspect in the overall structural design for tuning and controlling distance-dependent CT, whereby intermolecular interactions and self-assembly determine charge separation in thin films. The understanding and

S. Lucas,[+] Dr. E. Mena-Osteritz, Prof. P. Bäuerle
Institute of Organic Chemistry II and Advanced Materials
University of Ulm
Albert-Einstein-Allee 11, 89081 Ulm, Germany
E-mail: peter.baeuerle@uni-ulm.de

The ORCID identification number(s) for the author(s) of this article can be found under https://doi.org/10.1002/solr.202000653.

[+]Present address: Nvision Imaging Technologies GmbH, Albert-Einstein-Allee 11, 89081 Ulm, Germany

J. Kammerer, Prof. R. R. Schröder
3DMM2O – Cluster of Excellence (EXC-2082/1 – 390761711) and CAM – Centre for Advanced Materials
Heidelberg University
69177 Heidelberg, Germany

Dr. M. Pfannmöller
CAM – Centre for Advanced Materials
Heidelberg University
69177 Heidelberg, Germany

Y. He, Dr. N. Li, Prof. C. J. Brabec
Institute of Materials for Electronics and Energy Technology (i-MEET)
Friedrich-Alexander-Universität Erlangen-Nürnberg
Martensstrasse 7, 91058 Erlangen, Germany

Dr. N. Li, Prof. C. J. Brabec
High Throughput Methods in Photovoltaics

combination of both effects is essential for the development of efficient optoelectronic devices.[4]

Covalently linked molecular D–A systems have been used early in the development of organic photovoltaics as the solely photoactive component in solution-processed single-material organic solar cells (SMOSCs) with the aim to reduce the complexity of the cell fabrication process and facilitate control over nanoscale morphology and the D–A interface formation.[6,7] However, in contrast to the widely investigated bulk heterojunction organic solar cells (BHJ-OSCs), which very recently reached over 17% power conversion efficiency (PCE) in lab-scale devices but typically involve extensively optimized binary or even more complex ternary mixtures of D and A,[8] efficiencies for SMOSCs remained mostly below 2%.[9] The construction principle for photoactive single materials can be best divided into polymeric and oligomeric molecular D–A systems, bearing either flexible, insulating, or rigid, π-conjugated linkers.[10] Among them, the so-called "double-cable" polymer approach represents the farthest investigated D–A architecture and typically comprises a π-conjugated polymeric chain as the donor part and an acceptor unit, either fullerenic or nonfullerenic, that are attached to the polymeric backbone via flexible linkers. In this respect, Li and coworkers very recently improved the PCE of SMOSCs to an impressive 8.4% by developing a new "double-cable" polymer constructed of a benzodithiophene-based donor backbone with appended naphthalene diimides.[11] Interestingly, a thermally driven phase separation into lamellar structures was achieved at higher temperatures for a similar type of polymer, leading to an unexpectedly high thermal and light stability[12]

so far inconceivable for solution-processed binary or ternary BHJ-OSCs.

Various molecular or oligomeric D–A dyads and triads were developed and tailored for application in SMOSCs, typically comprising conjugated backbones based on oligo(phenylenevinylenes) or oligothiophenes, which bear fullerenic or PDI-type pendant groups.[10] Very recently, Min and coworkers reported a D–A dyad consisting of a benzodithiophene-cored oligothiophene, which was linked to a PC$_{71}$BM fullerene by a 12-atom spacer, reaching a PCE of 3.22%.[13] These results indicate that well-chosen spacers can be favorable elements for D–A systems in SMOSCs by facilitating favorable lamellar nanophase separation of D and A units. We recently developed a D–A dyad comprising a dithienopyrrol (DTP)-cored oligomeric donor, which was covalently linked to PC$_{61}$BM through a ten-atom alkyl ester spacer, and reported a PCE of 3.4% in SMOSCs.[14] In this novel molecular design, components of the well-performing biphasic BHJ-OSC system, oligomer 16 as donor blended with PC$_{61}$BM as acceptor, were covalently linked to form molecular materials for use as the sole photoactive component in SMOSCs (**Figure 1**).[15–17]

In this work, we now describe the structural variation and full characterization of this novel D–A dyad design by varying the chain length of the flexible spacer, resulting in a series of dyads 1–3 with 8, 10, and 12 atoms separating the donor and acceptor (Figure 1). Already presented results on dyad 2 are partly included here for comparability. In particular, we focused on the influence of the spacer length in D–A dyads on thermal, optoelectronic, photovoltaic, and charge transport properties to address correlations among each other. We also were interested to investigate the
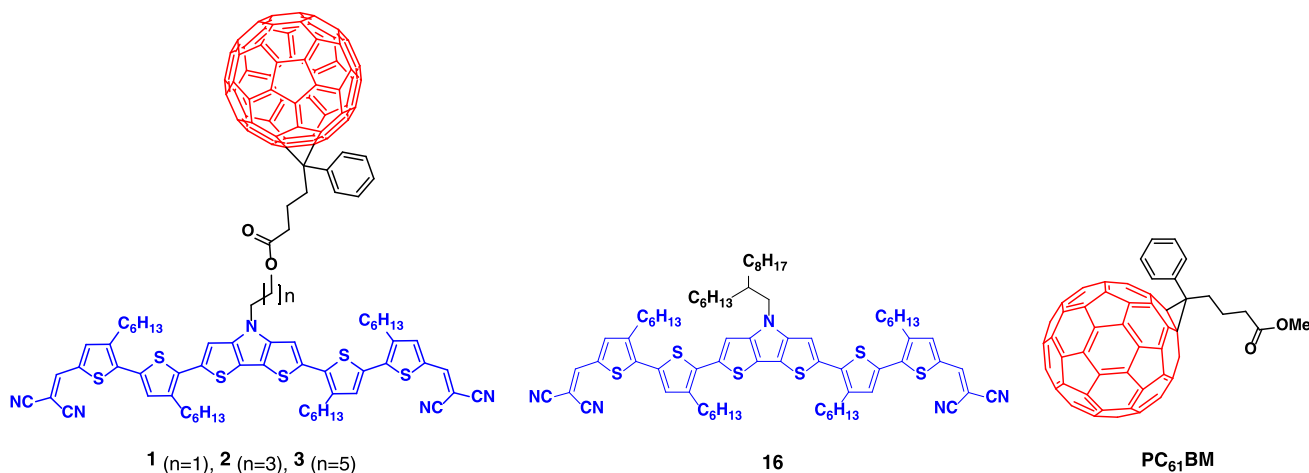

Figure 1. Basic structures of targeted donor–acceptor dyads 1 ($n = 1$), 2 ($n = 3$),[14] and 3 ($n = 5$) with spacer chain lengths of 8, 10, and 12 atoms between the donor and acceptor units (left); reference donor oligomer 16 (middle); and reference acceptor fullerene PC$_{61}$BM (right).

Helmholtz-Institute Erlangen-Nürnberg for Renewable Energy (HI ERN)
Immerwahrstr. 2, 91058 Erlangen, Germany

Dr. T. Leydecker, Prof. P. Samorì
Institut de Science et d'Ingénierie Supramoléculaires (ISIS)
University of Strasbourg, CNRS
8 allée Gaspard Monge, 67000 Strasbourg, France

Dr. T. Marszalek, Prof. W. Pisula
Molecular Electronics

Max Planck Institute for Polymer Research
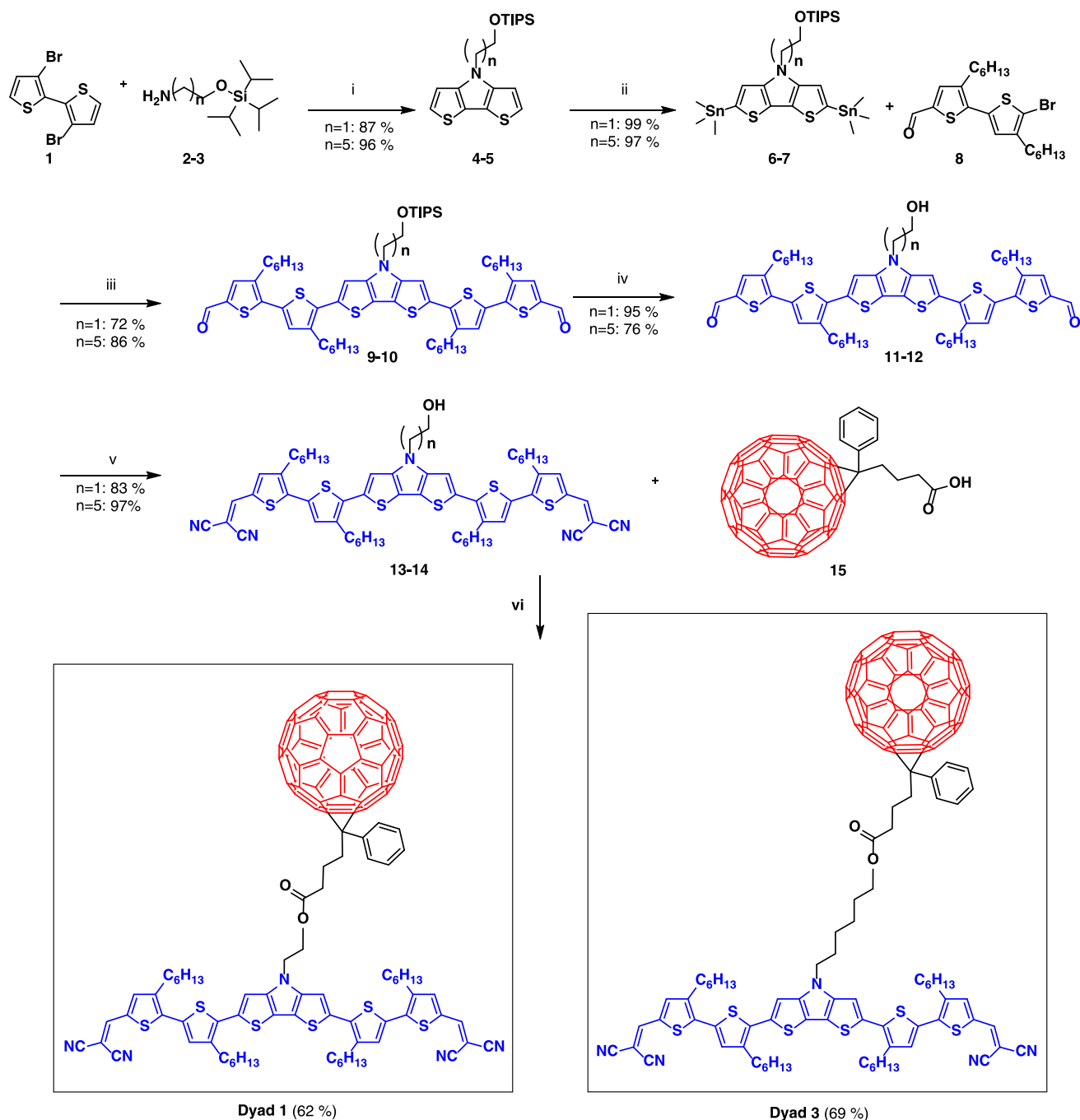Ackermannweg 10, 55128 Mainz, Germany

Dr. T. Marszalek, Prof. W. Pisula
Department of Molecular Physics
Faculty of Chemistry
Lodz University of Technology
Zeromskiego 116, 90-924 Lodz, Poland

surface and bulk nanomorphology of photoactive films and their changes upon post-treatment by solvent vapor annealing (SVA). In this respect, transmission electron microscopy (TEM), atomic force microscopy (AFM), and grazing incidence wide-angle X-ray scattering (GIWAXS) were applied and finally a theoretical model of the supramolecular order of the dyads was established, explaining the formation of D–A interfaces and phase-separated morphology, which are indispensable for a functioning solar cell.

2. Results and Discussion

2.1. Synthesis and Structural Characterization of D–A Dyads 1–3

The general synthetic route to the targeted D–A dyads with varying alkyl ester chain lengths, which was already established for dyad **2**,[14] is shown in **Scheme 1** and detailed synthetic procedures are given in Supporting Information (SI). Among the

Scheme 1. Synthesis of D–A dyads **1** and **3**: i) Pd$_2$(dba)$_3$, BINAP, NaOtBu, toluene, 110 °C, 24 h; ii) 1. n-BuLi, THF, 78 °C, 2 h, 2. Me$_3$SnCl, THF, −78 °C to r.t., 24 h; iii) Pd(PPh$_3$)$_4$, DMF, 85 °C, 24 h; iv) THF:HCl (10%) 50 °C, 5 h; v) malononitrile, NH$_4$OAc, DCE, 80 °C, 48 h; vi) EDC × HCl, DMAP, TEA, CS$_2$/DCB, 4d, 40 °C.

various possibilities to functionalize fullerenes, we considered the esterification of readily available fullerene carboxylic acid (PC$_{61}$BA) **15** with alcohols. Hydroxyalkylated DTPs are rarely described in the literature, and Lutkenhaus et al. recently published the synthesis of DTP-propan-1-ol.[18] We reacted 3,3'-dibromo-2,2'-bithiophene **1** with α,ω-(triisopropylsilyloxy) alkylamines **2** and **3** in twofold Pd-catalyzed Buchwald-Hartwig aminations to provide *N*-functionalized DTPs **4–5** in yields of 87–96% (Scheme 1). Twofold lithiation of DTPs **4–5** with *n*-BuLi and subsequent stannylation with trimethyltinchloride gave metallated intermediates **6–7** in nearly quantitative yields. These were coupled with brominated bithiophene aldehyde **8**[19] in Stille-type cross-coupling reactions to furnish oligomeric dialdehydes **9–10** in yields of 72–86%. The effective removal of the TIPS (triisopropylsilyl)-protecting groups with THF/HCl (10%) led to hydroxyl-functionalized oligomers **11–12**. In the next step, the terminal formyl groups were converted to dicyanovinylene (DCV) by Knoevenagel condensations with malononitrile to form donor blocks **13–14** in yields of 83–97% comprising ethan-1-ol and hexan-1-ol side chains, respectively, at DTP-nitrogen. In a final step, alcohols **13–14** were esterified with fullerene carboxylic acid PC$_{61}$BA **15** to targeted D–A dyads **1** and **3** in yields between 62% and 69% by in situ activation with 1-ethyl-3-(3-dimethylaminopropyl)carbodiimide (EDC) under basic conditions. The elaborated synthetic procedure over six steps delivered the D–A dyads in good overall yields of 27–34%, starting from commercially available reagents, and will allow for efficient upscaling. The structures of all novel precursors and dyads were confirmed by ^{1}H- and ^{13}C-NMR spectroscopy (Figure S2–S14, Supporting Information) and high-resolution mass spectra (HRMS) (Figure S15–S21, Supporting Information).

2.2. Thermal Properties of D–A dyads 1–3

Despite the melting points of the precursor alcohols **13–14** ranged between 210 and 213 °C, for dyads **1–3** relatively broad melting ranges beginning at much lower temperatures (**1**: 100–110 °C; **2**: 105–115 °C[14]; **3**: 120–130 °C) were found which were determined by differential scanning calorimetry (DSC) (Figure S22, Supporting Information). Due to the flexible linkage between the rather planar π-conjugated donor backbone and the movable spherical fullerene "ball," crystallization is obviously suppressed. A similar behavior has been noted for other D–A dyads having fullerene pendant groups separated by about the same spacer length.[20,21] For these cases, signals in DSC or powder diffraction were only seen for longer spacers in D–A molecules.[20,22] The dyads are thermally very stable and showed decomposition ranges above 392 °C (@ 5% mass loss) measured by thermal gravimetric analysis (TGA) (**Figure 2**).

2.3. Optical and Redox Properties of D–A Dyads 1–3 in Solution

All three dyads **1–3** are well soluble in organic solvents and solubilities in chloroform range from 70 to 80 mg mL^{-1}, guaranteeing the investigation of optical and redox properties and preparation of thin films for SMOSCs (vide infra). The optical
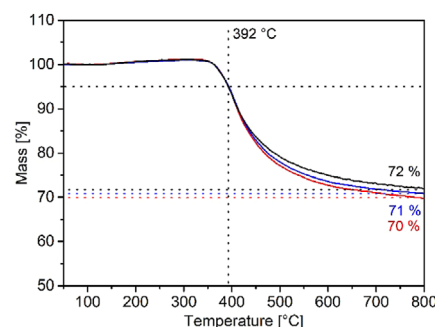

Figure 2. TGA traces of dyad **1** (black curve), **2** (blue curve),[14] and **3** (red curve) with a heating rate of 10 °C min^{-1} (right).

properties of the three D–A dyads **1–3** were investigated by UV–vis and fluorescence spectroscopy in dichloromethane (DCM) solutions at room temperature and compared with corresponding reference donors **13**, **14**, and **17** without the pending fullerene unit and with reference acceptor PC$_{61}$BM (**Table 1**).

In solution, the absorption spectra of dyads **1–3** are nearly identical and the absorption profiles reflect a superimposition of the spectra of the individual subunits, i.e., hydroxyalkylated precursors **13**, **14**, **17**, and PC$_{61}$BM. Thus, three absorption bands are visible for each dyad, the most prominent one at around 560 nm corresponds to a transition with CT character and the second weaker band at around 400 nm originates from a pure π−π* transition of the oligothiophene backbone. The maxima of both bands are practically identical to those of the donor references. The third band at around 330 nm is assigned to the pendant fullerene in the dyads and is comparable with the main absorption band of PC$_{61}$BM. The onset of absorption at the low-energy side of the spectra was at around 680 nm, leading to optical energy gaps of ≈1.8 eV. The emission maxima were found in the regime at around 800 nm and arise from the excitation of the oligomeric donor unit. Absorption and emission spectra of dyad **1**, reference donor **13**, and PC$_{61}$BM are exemplarily shown in **Figure 3** (left), and the corresponding data sets for dyad **2** and **3** are found in the SI (Figure S23 and S24, Supporting Information).

The electrochemical properties of the three dyads **1–3**, precursors **13**, **14**, **17**, and PC$_{61}$BM were investigated by cyclic

Table 1. Optical data of D–A dyads **1–3**, reference derivatives **13**, **14**, **17**, and PC$_{61}$BM in solution.

Oligomer	$\lambda_{max}^{sol\ a)}$ [nm]	ε [M^{-1} m^{-1}]	λ_{onset}^{sol} [nm]	E_g^{sol} [eV]	λ_{max}^{em} [nm]
1	<u>562</u>, 395, 328	57062	684	1.81	812
2[b]	<u>562</u>, 395, 328	55738	686	1.81	812
3	<u>566</u>, 397, 327	56200	690	1.80	778
13	<u>558</u>, 398	49800	676	1.83	816
17[c]	<u>562</u>, 399	52050	684	1.81	810
14	<u>568</u>, 402	50000	688	1.80	780
PC$_{61}$BM	329	46000	421	2.76	–

a)Absorption spectra were measured in dichloromethane solution, maximum underlined; b)Reference[14]; c)Derivative **17** corresponds to precursor **8** in ref. [14].
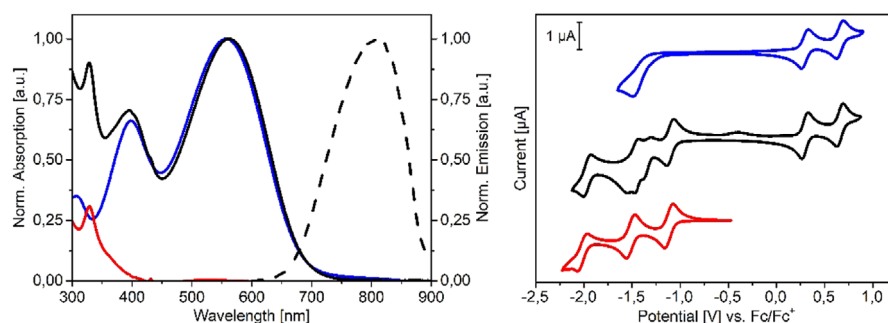
Figure 3. Absorption (black solid curve) and emission spectrum (black dotted) of dyad **1**, absorption for reference derivative **13** (blue), and PC$_{61}$BM (red) measured in dichloromethane solution (left); cyclic voltammogram of dyad **1** (black, middle), reference derivative **13** (blue, top), and PC$_{61}$BM (red, bottom) in dichloromethane ($c \approx 1 \times 10^{-3}$ M), TBAPF$_6$ as the supporting electrolyte (0.1 M), scan speed 100 mV s^{-1}. Potentials were referenced against the internal standard ferrocene/ferricenium (Fc/Fc$^+$).

Table 2. Electrochemical data of dyads **1–3**, reference derivative **13**, **14**, and **17**, and PC$_{61}$BM. Cyclovoltammogramms were measured in dichloromethane ($c \approx 1 \times 10^{-3}$ M), TBAPF$_6$ as the supporting electrolyte (0.1 M), scan speed at 100 mV s^{-1} at room temperature.

Oligomer	$E_{1/2}^{Ox\ 1,2}$ [V]	$E^{Ox\ onset}$ [V]	$E_{1/2}^{Red\ 1,2,3,4}$ [V]	$E^{Red\ onset}$ [V]	HOMO[a] [eV]	LUMO[a] [eV]	$E_g^{CV\ a)}$ [eV]
1	0.30, 0.66	0.23	−1.10, −1.34, −1.44, −1.97	−1.02	−5.33	−4.08	1.25
2[b]	0.25, 0.61	0.20	−1.14, −1.39, −1.52, −2.02	−1.07	−5.30	−4.03	1.27
3	0.29, 0.66	0.22	−1.10, −1.38, −1.46, −1.97	−1.04	−5.32	−4.06	1.26
13	0.30, 0.66	0.21	−1.29[d]	−1.30	−5.31	−3.80	1.51
17[c]	0.23, 0.61	0.16	−1.27[d]	−1.37	−5.26	−3.73	1.53
14	0.19, 0.57	0.12	−1.30[d]	−1.41	−5.22	−3.69	1.53
PC$_{61}$BM	–	–	−1.12, −1.51, −2.01	−1.04	−6.16[e]	−4.06	2.10[e]

[a]Calculated from onset values of the first oxidation and reduction waves by setting the HOMO energy of ferrocene to −5.1 eV versus vacuum; [b]Reference[14]; [c]Derivative **17** corresponds to precursor **8** in ref. [14]; [d]Irreversible peak, potential calculated according to Equation $I_{1/2} = I_p \times 0.865$; [e]Calculated using the optical energy gap.

voltammetry (CV) in dichloromethane solution and tetrabutylammonium hexafluorophosphate (0.1 M) as the supporting electrolyte. Data are given in **Table 2** and the representative CVs for dyad **1**, reference donor **13**, and PC$_{61}$BM are shown in Figure 3 (right). CVs for dyads **2** and **3** are found in the SI (Figure S25, Supporting Information). As in the optical investigation, the CV profiles of the dyads reflect a superimposition of the redox processes of the individual donor and acceptor references. Typically, two reversible oxidation waves with potentials of 0.19–0.30 and 0.57–0.66 V, respectively, were identified for **1–3** and **13**, **17**, and **14** and correspond to the formation of stable radical cations and successively dications located at the extended donor unit. From the onset potential of the first oxidation wave, highest occupied molecular orbital (HOMO) energies from −5.22 to −5.33 eV were calculated. In the reductive potential regime, the CVs of the dyads showed four reversible reduction waves, from which the middle two were overlaid. The assignment was possible by comparison with the potentials of the reference compound. Thus, reduction waves 1, 3, and 4 are assigned to the reduction of the fullerene subunit and well coincide with those of PC$_{61}$BM, leading to lowest unoccupied molecular orbital (LUMO) energies from −4.03 to −4.08 eV, which were determined from the onset of the first reduction wave. The second wave can be assigned to the reduction of the DCV groups

in the donor backbone and correlates to those of reference derivatives **13**, **17**, and **14**, which do not bear a fullerene unit. Therefore, their LUMO energies are raised from −3.69 to −3.80 eV and compared with the dyads somewhat larger energy gaps of ≈1.5 eV occur. Due to their strong absorption in the visible region from 400 to 850 nm and well-located energy levels of the frontier orbitals, dyads **1–3** represent good candidates for application in organic solar cells.

2.4. Photovoltaic Properties and Solar Cell Performance

The novel D–A dyads **1–3** were implemented and optimized as the sole photoactive component in SMOSCs with the simplified and standard device structure glass/ITO/PEDOT:PSS/ dyad **1–3**/ LiF/Al. SMOSCs were prepared in ambient conditions by spin coating a 15 mg mL^{-1} solution of the dyads in chloroform and were individually optimized in the pristine state and after post-treatment by SVA using various solvents such as tetrahydrofurane (THF), chloroform (CHCl$_3$), or carbon disulfide (CS$_2$) and exposure times. As already mentioned earlier, SVA substantially improved the photovoltaic performance of biphasic BHJ-OSCs comprising blends of model donor **16** and PCBM as the acceptor by positively affecting the nanomorphology and phase separation.[15–17] The first results for dyad **2** in SMOSCs confirmed that

the impact of SVA and PCE was nearly doubled.[14] Similar to the biphasic BHJ-OSCs, for all three dyads **1–3**, the best results were obtained for layer thicknesses of 100 ± 5 nm (spin coating @ 1500 rpm, Table S1, Supporting Information) and for a relatively short, but well-reproducible SVA impact time of 20–30 s (Table S2, Supporting Information). The measured photovoltaic parameters of the optimized pristine SMOSCs and those, which were post-treated with carbon disulfide (CS_2) for 30 s exposure time, are shown for comparison in **Table 3**. Detailed data for the optimization of the various parameters are shown in Table S1–S5, Supporting Information. The current density–voltage (J–V) curves of optimized SMOSCs with pristine photoactive layers are shown in **Figure 4** (left), corresponding J–V curves after SVA in Figure 4 (right).

SMOSCs comprising as-cast photoactive layers showed a dependency of the spacer length in dyads **1–3** on photovoltaic parameters. With increasing chain length, except the open-circuit voltage (V_{OC}), which only slightly varied, short-circuit current density (J_{SC}), fill factor (FF), and the resulting PCE are continuously increased finally leading to 2.9% PCE for dyad **3** comprising the longest spacer. Post-treatment of the devices by SVA with CS_2 for 30 s enhanced the crystallinity of the active films in all cases, indicated by the slight decrease in V_{OC} and increase in other photovoltaic parameters. The major improvement was found for dyad **1** (shortest spacer) with a fourfold increase of the PCE from 1.06% to 4.26% mainly due to the higher J_{SC} of 11.53 mA cm^{-2} and FF of 0.46 (Table S3,

Supporting Information). This optimized PCE currently represents the best value for oligomeric systems in SMOSCs and surpasses many of the polymer-based devices. The smallest changes were found for dyad **3**, which improved from 2.9% PCE to 3.37% (Table S5, Supporting Information), those for dyad **2** were intermediate (1.66–2.8% PCE). It should be noted here that for dyad **2** SVA with chloroform for 25 s gave, with 3.39% PCE, a slightly better result (Table S4, Supporting Information).[14]

Despite the different spacer lengths in our dyads, FFs of the optimized as-cast and post-treated devices stayed in a relatively low and narrow regime (0.30–0.40 and 0.41–0.46, respectively), indicating that the geminate and nongeminate recombination of charge carriers seems to be the main deactivation pathways due to the inherent small geometric gap between the donor and acceptor (vide infra).[23,24] On the other hand, the largest difference among the dyads is noted in J_{SC} (4.04–8.82 mA cm^{-2} (as-cast), 8.64–11.53 mA cm^{-2} [SVA]) pointing to increased CT. The photoluminescence (PL) experiments for films of dyad **1** revealed that the emission intensity due to the oligothiophene donor part is progressively quenched and slightly blue-shifted (@ 936–895 nm) with increasing SVA time, indicating a more efficient CT (**Figure 5**, left). The energy of the CT state was determined by the electroluminescence (EL) measurement, revealing an absorption maximum at around 1080 nm (1.15 eV) (Figure 5, right).

If one compares the photovoltaic parameters of the best SMOSCs with dyad **1** after SVA with those of oligothiophene-PC$_{71}$BM after thermal annealing published by Nguyen

Table 3. Photovoltaic parameters of D–A dyads **1–3**, as-cast and after SVA with carbon disulfide (CS_2) for 30 s. Processing conditions: spin coating (@ 1500 rpm) solutions of 15 mg mL^{-1} at r.t. Average value for four devices $\pm$ standard deviation (best value); device architecture: glass/ ITO/PEDOT:PSS/ dyad **1–3**/LiF/Al.

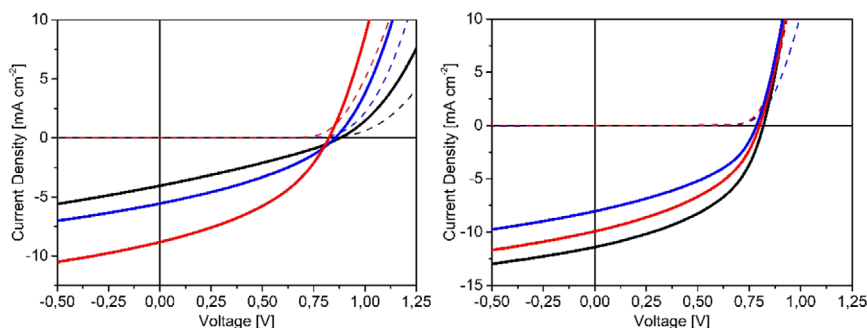| D–A dyad	SVA solvent [time]	V_{OC} [V]	J_{SC} [mA/cm^2]	FF	PCE [%]	EQE$_{max}$	J_{sc}^{EQE} [mA/cm^2]
1	–	0.88 ± 0.01 (0.88)	3.96 ± 0.05 (4.05)	0.30 ± 0.01 (0.30)	1.03 ± 0.01 (1.06)	0.24 @ 416 nm	3.79
2[a]	–	0.86 ± 0.01 (0.86)	5.38 ± 0.23 (5.55)	0.35 ± 0.01 (0.35)	1.60 ± 0.06 (1.66)	0.28 @ 410 nm	4.82
3	–	0.83 ± 0.01 (0.83)	8.75 ± 0.07 (8.82)	0.40 ± 0.01 (0.40)	2.88 ± 0.02 (2.90)	0.42 @ 417 nm	8.52
1	CS_2 (30 s)	0.82 ± 0.01 (0.82)	11.42 ± 0.08 (11.53)	0.45 ± 0.01 (0.46)	4.21 ± 0.05 (4.26)	0.48 @ 654 nm	11.85
2[a]	CS_2 (30 s)	0.80 ± 0.01 (0.81)	8.39 ± 0.26 (8.64)	0.41 ± 0.01 (0.41)	2.74 ± 0.08 (2.80)	0.41 @ 643 nm	9.07
3	CS_2 (30 s)	0.81 ± 0.01 (0.81)	9.86 ± 0.13 (9.94)	0.42 ± 0.01 (0.43)	3.34 ± 0.05 (3.37)	0.40 @ 679 nm	10.40

[a]Reference.[14]

Figure 4. J–V characteristics of optimized solar cells with dyads **1–3** as the photoactive layer using the cell architecture: glass/ITO/PEDOT:PSS/ dyad **1–3**/LiF/Al under 100 mW cm^{-2} AM 1.5G illumination (full lines) and in the dark (dotted lines) in the pristine state (left); after SVA (CS_2, 30 s) (right). Dyad **1** (black), dyad **2** (blue),[14] and dyad **3** (red).
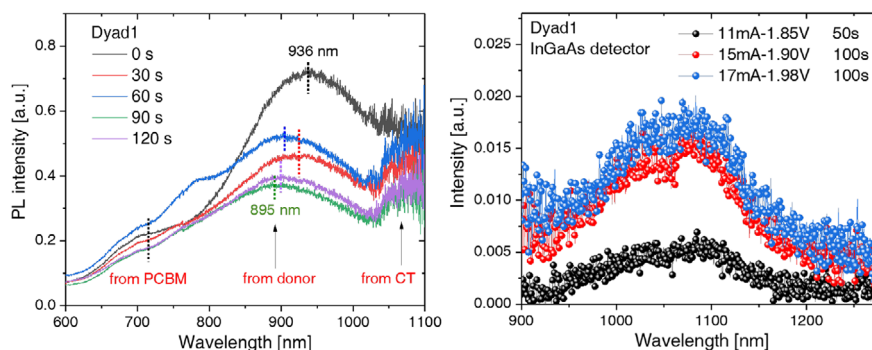
Figure 5. The PL film spectra of dyad **1** after 0–120 s of SVA time (excitation wavelength: 488 nm) (left); EL spectra of dyad **1**-based device using InGaAs detector with different current injection (right).

et al.,[25] we find that their couple delivers a higher V_{OC} (0.98 vs 0.82 V) due to a better stabilized HOMO energy value (-5.45 vs -5.33 eV) at about the same FF (0.44 vs 0.46). However, their lower PCE (3.22% vs. 4.26%) mainly arises from the substantially reduced photocurrent (7.50 vs 11.53 mA cm^{-2}) at about the same active layer thickness. As already pointed out, nevertheless, in both cases, the FF of the SMOSCs is relatively low and limits the PCE compared with biphasic BHJ-OSCs.

To obtain information on the charge generation process, external quantum efficiencies (EQE) were measured for the optimized as-cast and SVA-treated devices. The impact of SVA is best seen for devices of dyad 1, whereupon EQE was more than doubled, reaching almost 50% @ 420 nm and @ 650 nm after SVA (**Figure 6**, left). The EQE spectra of dyads **2** and **3** are shown in the SI (Figure S26 and S27, Supporting Information). In accordance with the photovoltaic data they reveal smaller changes, in particular for dyad **3**. J_{SC} values obtained by the integration of the EQE spectra are well comparable with those obtained from the *J–V* curves.

Thus, one can rationalize from these results that upon SVA the morphology of the photoactive layer is positively influenced and a certain rearrangement of the D–A molecules occurs. This effect obviously depends on the spacer length of the dyads and is largest for dyad **1** with the shortest spacer and least for **3** with the longest one. Without any post-treatment, dyad **3** showed the highest efficiency (2.90%), and we assume that in pristine films, better packing of both subunits is allowed due to the higher

flexibility of the longest linker in the series, which may act as an internal solvent.

This trend was retrieved in the UV–vis film spectra of the dyads before and after SVA: dyad **1** showed the largest bathochromic shift of the absorption bands, dyad **3** the smallest concomitant with the larger and smaller rearrangement of the donor units after SVA, respectively (**Table 4**). Thin films of dyads **1–3** were prepared by the spin coating of chloroform solutions on glass slides and investigated before and after SVA. Compared with solution spectra, the film spectra generally exhibited peak broadening and distinct red-shifts of about 40–80 nm for the bands corresponding to the donor moieties indicating $\pi-\pi$ interactions in the solid state, whereas the fullerene band was only slightly shifted. The absorption bands cover a broad range from 400 to 850 nm and consequently the optical energy gap is reduced to $\approx$1.5–1.56 eV for **1–3** and the reference derivatives **13**, **14**, **17**, and PC$_{61}$BM, which are compared. The film absorption spectrum of dyad **1** is shown in Figure 6 (right) and although the absorption profile reflects a good superimposition of the spectra of the individual subunits (donor **13** and PC$_{61}$BM), the slight blue-shift of the low-energy band in **1** compared to reference **13** indicates a perturbing effect of the fullerene to the inherent packing ability of the oligomeric donor.[13] For dyads **2** and **3** the individual blue-shifts are smaller (Figure S28 and S29, Supporting Information).

In the UV–vis film spectra of dyads **1–3** after SVA, we find small bathochromic shifts to 419–429 nm ($\Delta\lambda=$ 3–11 nm) for the $\pi-\pi^*$ band and substantially larger ones to 647–660 nm
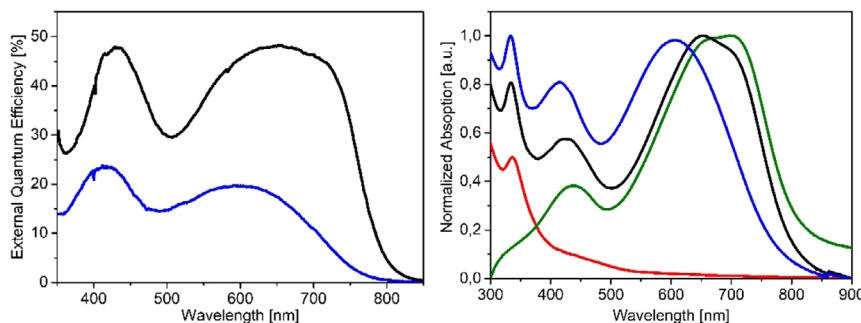

Figure 6. EQE spectra of the best-performing solar cells of dyad **1** before (blue) and after SVA (black) (left); thin-film absorption spectra of dyad **1** before (blue) and after SVA (black); and thin-film absorption of reference derivative **13** (green) and PC$_{61}$BM (red) (right).

Table 4. Optical data of D–A dyads **1**–**3**, reference derivatives **13**, **14**, **17**, and $PC_{61}BM$ in thin films as cast and after SVA.

Oligomer	As cast			After SVA		
	$\lambda_{max}^{film\,a)}$ (CoM)[b)] [nm]	λ_{onset}^{film} [nm]	E_g^{film} [eV]	$\lambda_{max}^{film\,c)}$ [nm]	$\lambda_{onset}^{film\,c)}$ [nm]	$E_g^{film\,c)}$ [eV]
1	604, 410, 332	808	1.53	647, 419, 333	802	1.55
2[d)]	630, 418, 334	794	1.56	660, 429, 333	803	1.54
3	647, 418, 332	805	1.54	656, 421, 334	805	1.54
13	698, 437 (665)	818	1.52	–	–	–
17[e)]	661, 434 (661)	816	1.52	–	–	–
14	668, 438 (669)	812	1.50	–	–	–
$PC_{61}BM$	338	540	2.10	–	–	–

[a)]Thin films were produced by spin coating from chloroform solution on glass slides; [b)]Center of mass (CoM) of the low-energy band; [c)]Thin-film data after SVA; [d)]Reference [14]; [e)]Derivative **17** corresponds to precursor **8** in ref. [14].

($\Delta\lambda = 9$–43 nm) for the intramolecular CT band of the donor subunit concomitant with a hyperchromic effect (Table 4). The absorption of the fullerene unit at 332–334 nm remained unaltered (Figure 6, right, for **1**, Figure S28, Supporting Information, for **2**, Figure S29, for **3**, Supporting Information). The largest red-shifts and the largest impact of SVA were found for dyad **1**, comprising the shortest spacer and the band maxima approach those of the unperturbed reference compound **13**. We therefore rationalize that SVA mainly affects the reorientation of oligomeric donor segments by π-stacking and decreased distance between the π-conjugated donors. In the case of dyad **3** (longest spacer), only a small red-shift of the absorption maxima is observed for the SVA-treated films, indicating in accordance with the photovoltaic data, only minor reorientation of the molecules in the film (Table 4, Figure S29, Supporting Information).

2.5. Thermal and Illumination Stability of SMOSCs

SMOSCs are endowed with an intrinsic stability advantage over BHJ-OSCs due to the covalently bound D–A materials in the active layer, in which the donor and acceptor cannot demix.[9] In this respect, the stability tests of SMOSCs of our dyads **1**–**3** were undertaken in nitrogen atmosphere in a specifically engineered air-tight measurement holder. For thermal stability tests, the solar cells were kept at 90 °C in the dark which is below the melting points of the dyads, whereas for illumination stability tests, solar cells were irradiated under light emitting diode (LED) light at room temperature. The spectrum of the LED light source is pictured in Figure S30, Supporting Information. In the beginning, SMOSCs with the conventional layer structure ITO/PEDOT:PSS/dyad **1**–**3**/Ca/Al were used for stability tests. All three dyads showed obvious burn-in degradation. Both, J_{SC} and FF, were affected under thermal and light stress (Figure S31, S32, Supporting Information), with only around 50–70% of the initial efficiency remaining after 200–300 h of testing. This effect is mainly caused by the degradation of interface layers used in this cell architecture. Therefore, an inverted cell structure ITO/ZnO/dyad **1**–**3**/MoO_x/Ag was adopted for further stability investigation to reduce the destabilizing influence of the interfaces. SMOSCs built with inverted architecture showed comparable performance and the same trend after SVA was compared with the conventional structure: dyad **1** (PCE 3.75%) > **2** (PCE 3.56%) > **3** (PCE 3.33%) (Table S6 and Figure S33, Supporting Information). As shown in **Figure 7**, all three dyads exhibited a substantially enhanced stability in SMOSCs compared with the normal device structure. Under thermal stress at 90 °C and in the dark, we observe very stable V_{OC} values and a significantly reduced burn-in degradation behavior for J_{SC} and FF within the first 50 h. Such burn-in might be due to dimerization of the fullerene acceptors, which is found in BHJ architectures; however, previous studies identified UV light as a major driving force for fullerene dimerization.[26] Interestingly, the individual dyads displayed a distinctly different stability behavior and order which appears to correlate with the spacer length: dyad **1** > dyad **2** > dyad **3**. After almost 400 h of aging, dyad **1**, **2**, and **3** kept 90%, 80%, and 60% of their original efficiency, respectively. Although interface-induced degradation cannot be completely ruled out, molecular rearrangement appears more likely because dyads with longer spacers resulted in reduced stability.

Because inverted SMOSCs with dyad **1** as the photoactive material showed the best intrinsic stability, we further tested this configuration under 1 sun LED illumination at room temperature. As shown in **Figure 8**, all photovoltaic parameters were very constant and did not show any decrease nor burn-in effect. This underlines the assumption that burn-in degradation as observed under thermal stress indeed is related to molecular rearrangements. Therefore, we conclude that dyad **1** is a very light-stable material with no signs of degradation after almost 600 h of light stress.

2.6. Charge Transport and Mobility Measurement

The electrical characteristics of D–A dyads **1**–**3** were investigated through the fabrication and characterization of organic field-effect transistors (OFETs) in bottom-contact bottom-gate configurations prior and after SVA treatment with CS_2 (**Table 5**).[27] In **Figure 9**, transfer curves in the logarithmic scale for dyad **1**–**3** before and after SVA post-treatment are shown. All transfer curves, i.e., under positive and negative gate bias in the linear and logarithmic scale, are reported in the SI (Figure S34,
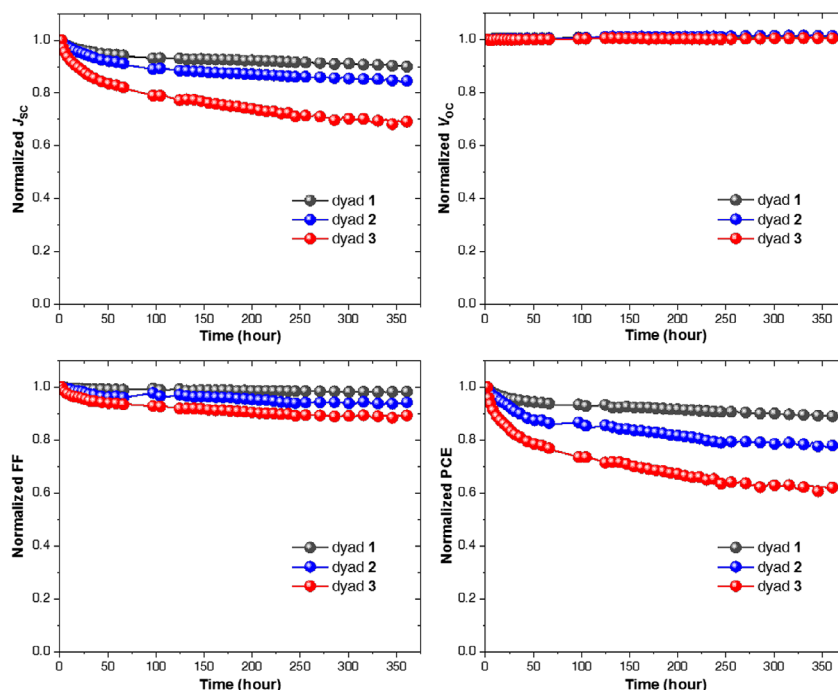
Figure 7. Stability test of dyads **1–3** in SMOSCs with the inverted layer sequence ITO/ZnO/dyad **1–3**/MoO$_x$/Ag: Evolution of photovoltaic parameters of optimized solar cells under thermal stress at 90 °C in the dark at r.t. in nitrogen atmosphere for 375 h (the empty range from around 70 to 120 h was due to program issues and pitfalls).
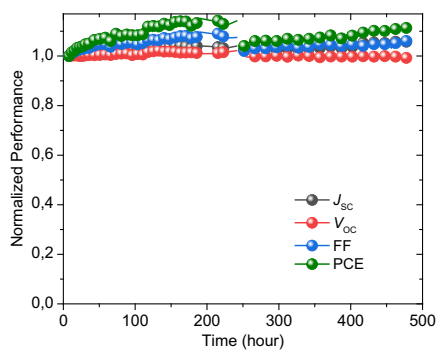

Figure 8. Stability test of dyad **1** in SMOSCs with inverted layer sequence ITO/ZnO/dyad 1/MoO$_x$/Ag: Evolution of photovoltaic parameters of optimized solar cells under LED illumination (1 sun intensity) at r.t. in nitrogen atmosphere for 600 h.

Table 5. Electrical characteristics of dyads **1–3**. Field-effect transistors prior to and after CS$_2$ post-treatment of 30 s. Average saturation regime field-effect mobility for holes (μ_p) and electrons (μ_n) and threshold voltage (V_{th}) of the devices prior to and after CS$_2$ treatment. Averages over four devices: two at $L = 5\,\mu m$ and two at $L = 10\,\mu m$.

D–A dyad	$\mu_{n,\,sat} \times 10^{-5}$ [cm^2/Vs]	V_{th} (electrons) [V]	$\mu_{p,\,sat} \times 10^{-5}$ [cm^2/Vs]	V_{th} (holes) [V]
1	2.95 ± 0.69	15 ± 2	0.23 ± 0.01	-5 ± 2
1 + SVA	9.61 ± 2.07	18 ± 3	7.02 ± 0.73	-1 ± 1
2[a]	2.86 ± 0.94	23 ± 3	0.47 ± 0.09	-6 ± 3
2 + SVA[a]	7.76 ± 3.14	30 ± 4	26.30 ± 2.99	7 ± 4
3	3.24 ± 1.06	17 ± 6	4.87 ± 3.03	1 ± 6
3 + SVA	6.06 ± 2.26	18 ± 4	27.51 ± 4.71	-3 ± 4

[a]Partly in ref. [14].

Supporting Information, dyad **1**, S35 dyad **2**, S36 dyad **3**). Transfer curves in the saturation regime revealed ambipolar charge transport for all three dyads prior to SVA treatment, with a high *n*-type mobility, albeit with a relatively low *p*-type mobility (0.23×10^{-5} and 0.47×10^{-5} cm^2 V^{-1}s^{-1} for dyad **1** and dyad **2**, respectively). Dyad **3** however featured a higher *p*-type mobility of about 5×10^{-5} cm^2 V^{-1}s^{-1}. While the *n*-type mobility is constant at around 3×10^{-5} cm^2 V^{-1}s^{-1} across all dyads, indicating no correlation between molecular structures, i.e., spacer length and electron transport, *p*-type mobility was found to increase with a longer spacer length, indicating that proximity between the

donor and acceptor moieties of the dyad is detrimental to *p*-type charge transport.

The important finding here is that the mobilities well correlate with photovoltaic parameters, which are shown in **Figure 10** for PCEs. Whereas dyads **1** and **2** featured lower PCEs (of 1.06% and 1.66%, respectively) and *p*-type mobilities, dyad **3** exhibited a higher PCE of 2.90% and highly balanced mobility values.

Upon SVA treatment with CS$_2$, significant changes in electrical performance are observed, in the form of an increase in both, *p*- and *n*-type mobilities, for each dyad, correlated with the
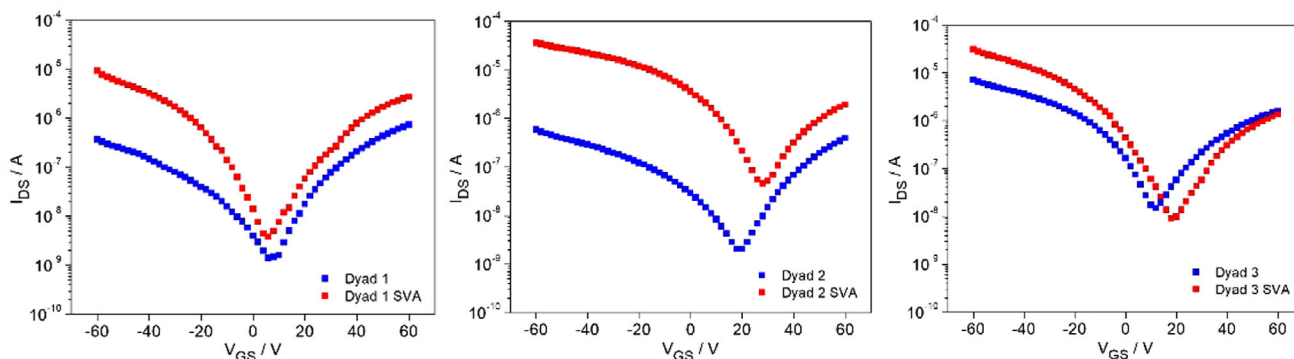
Figure 9. Transfer curves of dyads **1**–**3** devices prior and after SVA (CS$_2$) treatment [$V_{DS} = +60$ V, $L = 5$ μm, $W = 10$ mm, $C = 15$ nF cm^{-2}].
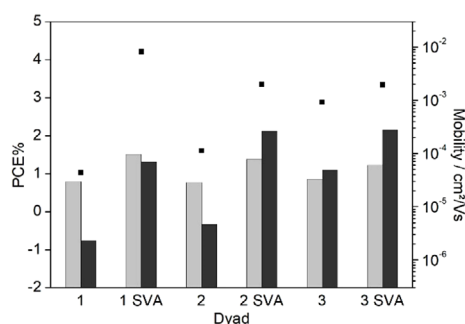

Figure 10. Average *n*-type mobility (light grey histograms), *p*-type mobility (dark grey histograms), and PCE% (black rectangles) of each dyad before and after CS$_2$ treatment. The PCE follows the same trend as *p*-type mobility.

increase in PCE in each case. These enhancements in mobility can be partially attributed to the intensified intermolecular packing by π–π-stacking of donor moieties, as was evidenced as well by film absorption spectra (Figure 6 and Figure S28, S29, Supporting Information) and GIWAXS patterns (**Figure 11**). The obtained mobility values of ≈10^{-4} (hole) and 10^{-4} cm^2 V^{-1}s^{-1} (electrons) are quite high for D–A dyads and come into the range of good biphasic morphologies of efficient BHJ-OSCs. Interestingly, while an increased spacer length still results in increased p-type mobility, the *n*-type mobility follows an opposed trend, i.e., it increases with a decreasing spacer length.

The trend in ambipolar charge transport versus photovoltaic performance reveals that a strong increase in a single parameter (*p*-type or *n*-type charge transport) does not translate into a major increase in PCE. This is exemplified by dyad **3** which, with a fourfold increase in *p*-type mobility, reaching the highest value among all dyads (2.7×10^{-4} cm^2 Vs^{-1}), does only achieve a low increase of PCE from 2.9% to 3.37%. On the other hand, the SVA of dyad **1** films led to a strong increase in mobility of both charge carriers, resulting in ambipolar devices with balanced mobilities and the highest PCEs of all tested dyads. These findings highlight how the PCE is tightly correlated with the charge transport capabilities of the tested semiconducting materials and how an adequate treatment aimed at increasing the performances of the lacking charge transport capability (in this case, *p*-type

mobility for dyad **1** and **2**) will result in substantial improvements of PCE. Despite charge mobilities in vertical direction are more important for solar cells and OFETs reflect charge transport parallel to to the substrate, the correlation here is straightforward, because the investigation of nanomorphology revealed that order and even more crystallinity in the dyad films are relatively moderate, even after SVA (vide infra).

Furthermore, the extracted electrical parameters indicate that charge transport can be modulated through molecular design, and adjusting the spacer length between the donor and acceptor moieties of the dyads will result in a modification of hole and electron mobility. An increased spacer length correlates with increased *p*-type and decreased *n*-type mobility. Hence, fine-tuning of the electrical and optoelectronic performance can be achieved at both stages, the synthesis stage and the processing stage. In comparison, the best-performing "double-cable" polymers showed a significantly enhanced hole and electron mobility upon thermal annealing; however, no balance of the carriers was achieved and hole mobility always was higher by two to three orders of magnitude.[11,12]

2.7. Film Morphology

2.7.1. Transmission Electron Microscopy (TEM)

To gain information on bulk morphology, films of the best-performing dyad **1**, parent donor oligomer **16**, and fullerenic acceptor PC$_{61}$BM were investigated by TEM. Thin films of dyad **1** were used as cast and after 10, 30, and 60 s of post-treatment by SVA with CS$_2$ to see the evolution of the morphology changes upon SVA. In analytical TEM (ATEM), material-specific electron energy loss signals from electron spectroscopic imaging (ESI) have been proven to effectively reveal the morphology of organic photovoltaic blends at the nanoscale.[28] The distinct volume plasmon signals of reference **16** and PC$_{61}$BM between 8 and 40 eV in the electron energy-loss spectra (EELS) would yield strong contrast between different material domains due to different volume plasmon signals (Figure 11a, left). We showed in a previous work for binary blends of **16** and PC$_{61}$BM that nanometer-sized domains in the range of ≥5 nm can be visualized by ESI in this energy-loss range.[16,29] However, for thin films of dyad **1**, only thickness-related contrasts were observed and no demixing into donor- and acceptor-rich domains was detected
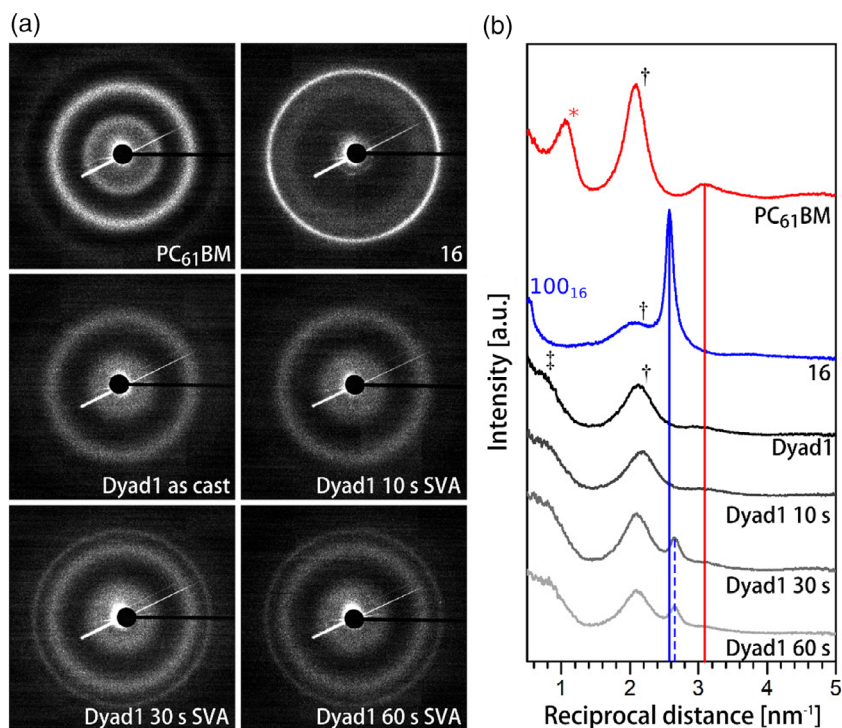
Figure 11. The analytical TEM results of dyad 1 and molecular references **16** and PC$_{61}$BM. a) Diffraction patterns of references PC$_{61}$BM and **16** (top) and films of dyad **1** in the as-cast state and after 10, 30, and 60 s of SVA (middle, bottom) from SAED. c) The corresponding radial-averaged profiles. Vertical lines indicate the π-stacking distance of **16** (blue solid), dyad **1** (blue dashed), and the aggregation of fullerene units (red solid). Bright streaks in the diffraction patterns are caused by the opening beam shutter when working in low-dose conditions and were excluded from the radial profiles.

(Figure 11a, left, Figure S37, S38, Supporting Information). Therefore, either complete D–A mixing occurs which would be detrimental for PV, or any structural feature would be well below 5 nm which is very likely due to the small size of the molecules (<2 nm) and the covalently linked D and A units in the D–A dyads. Low contrast in TEM and crystalline domains <10 nm were as well described for a diketopyrrolopyrrole–perylenediimide 'double-cable' polymer.[30]

Nevertheless, selective-area electron diffraction (SAED) patterns showed the presence of aggregation and separation on the molecular level (Figure 11). All patterns exhibited broad peaks, indicating amorphous films or nanosized crystallites. The ring pattern of PC$_{61}$BM is in agreement with our GIWAXS data (vide infra) and with results from Yang et al., who showed that the broad rings can originate from the superposition of different lattice spacings.[31] The correlation of the observed peaks with the theoretically calculated diffractogram of PC$_{61}$BM[32] revealed that the peak at about 1 nm^{-1} (1 nm spacing; Figure 11b,*) is composed of the (110), (111), (101), and (002) reflections (data in Figure S39, Supporting Information). However, in the context of less-ordered systems, it is more appropriate to refer to molecules and distances instead of lattice planes and crystallographic axes. Therefore, the distance of about 1 nm corresponds to the center-to-center distances of fullerene units, which have a diameter of about 0.7 nm. The broad peak at about 3.1 nm^{-1} (red line) corresponds to the 0.32 nm wall-to-wall distance of two adjacent fullerene units. This agrees with the

expected value of 0.3193 nm from the single-crystal structure (cf. Figure S39, Supporting Information). The ring pattern of donor reference **16** shows two sharp peaks at 0.5 and 2.6 nm^{-1}, which correspond to its 100$_{16}$ reflection[33] and π-stacking peak (blue solid line), respectively. This yields a π-stacking distance of 0.39 nm. An additional broad and minor peak is found at 2.0 nm^{-1} (0.5 nm spacing; †), which is also observed for PC$_{61}$BM and dyad 1.

Further comparing the diffraction patterns of the references with those of dyad **1**, a relatively broad background down to scattering distances of about 1.3 nm^{-1} (0.77 nm spacing; ‡) is observed. All diffractograms from dyad **1** contain noticeable contribution from the wall-to-wall coordination of the fullerene unit similar to the PC$_{61}$BM reference at around 3.1 nm^{-1} (Figure 11b, red line). This peak, and thus the wall-to-wall coordination, of the PC$_{61}$BM units is barely affected by SVA. The as-cast film of dyad **1** and the 10 s SVA-treated film did not show significant changes in the profile, whereas after 30 s of SVA a distinct peak at 2.6 nm^{-1} (0.37 nm spacing) evolved. This peak is associated with the aggregation of donor species during SVA and is hardly affected by further SVA treatment (60 s). This indicates that π-stacking of the oligomeric donor units emerges similar to the film of reference **16**, whereupon the stacking distance is decreased from 0.39 nm for **16** to 0.37 nm for D–A-linked dyad **1**. This enhanced ordering of the donor units through SVA is in accordance with the optical, charge transport, and photovoltaic data (vide supra).

2.7.2. AFM Measurement

To characterize and rationalize the impact of SVA on the nanomorphology of the photoactive layer of dyads **1–3**, we investigated the surface topology by means of tapping-mode AFM (**Figure 12**). The analysis of the topography images for the as-cast films of the three dyads (labeled T in Figure 12a,c,e) revealed a tightly packed finest morphology, comprising small structural features of 5–10 nm size and up to 15 nm in the case of dyad **3**. The surface roughness is calculated to be little ($\Delta^T = 8$ nm in case of dyad **2**) to moderate ($\Delta^T \approx 20$ nm for dyads **1** and **3**). In the phase images of dyads **1** and **2** (Figure 12a,c, right), the lack of contrast ($\Delta^{Ph} = 5$–$6°$) suggests a molecularly fine mixture of donor and acceptor units on the surface, supported by monotonous histograms (insets). On the contrary, dyad **3** showed a relevant phase contrast ($\Delta^{Ph} = 60°$) and a corresponding bimodal histogram, indicative of phase separation.

The SVA treatment of the dyads led to different morphological changes: in the case of dyad **3** slightly bigger structures of 10–20 nm diameter and some few crystallites of about 60 nm are visible in the topography image and a strong phase contrast,

$\Delta^{Ph} = 115°$, concomitant with a bimodal histogram are shown in the corresponding phase image (Figure 12f). An increase of aggregate size to 20–60 nm diameter has also been observed in the topography images of SVA-treated dyad **2** but still we found no evidence of the enhanced phase contrast on the surface of the active layer ($\Delta^{Ph} = 6°$ and monotonous histogram in Figure 12d). For dyad **1** SVA slightly increases the size of the aggregates to 18 nm in the topography and a relevant contrast, $\Delta^{Ph} = 60°$, appears in the phase image (Figure 12b). The two distinct phases can be distinguished as well in the inserted histogram, like in case of dyad **1**, indicating the presence of crystalline and amorphous regions on the surface of the active films. In summary, in the topography images of films of the three dyads **1–3** after SVA, the trend that bigger aggregates are formed is recognized, whereas the AFM phase images in more detail showed the influence of the spacer length and SVA on surface morphology of thin photoactive films.[33] Although these findings cannot be extrapolated to the bulk, they seem to be in accordance with the trends in transport properties and device performance and are of interest because so far AFM investigations on co-oligomeric dyads and triads typically did not
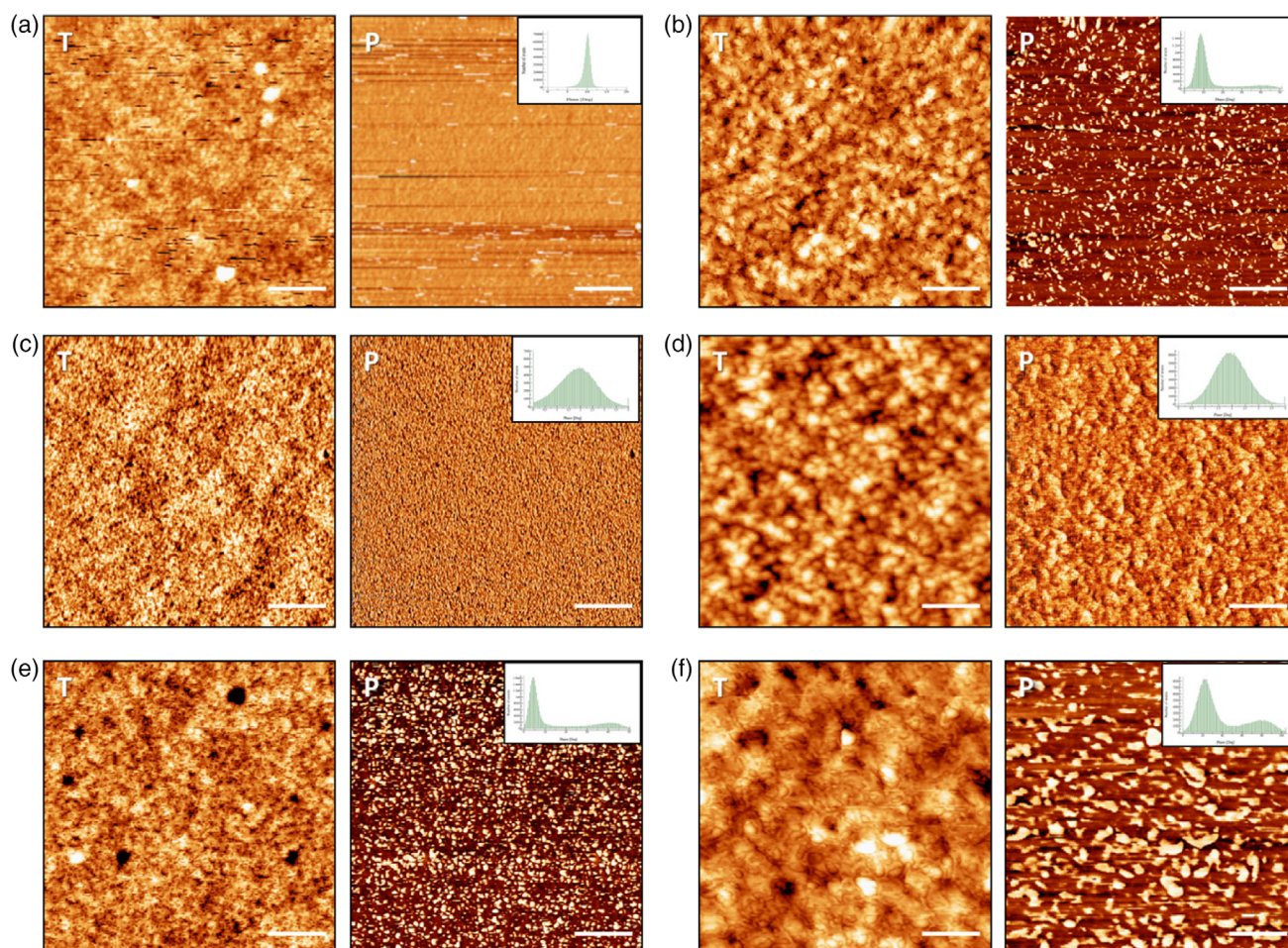

Figure 12. AFM topography (left, T) and phase images (right, P. Inset: histograms) ($1 \times 1 \mu m^2$) of dyad **1** a) as cast ($\Delta^{Topography}$ (Δ^T) = 20 nm, Δ^{Phase} (Δ^{Ph}) = 6°) and b) after SVA ($\Delta^T = 20$ nm, $\Delta^{Ph} = 60°$); dyad **2** c) before ($\Delta^T = 8$ nm, $\Delta^{Ph} = 5°$) and d) after SVA ($\Delta^T = 16$ nm, $\Delta^{Ph} = 6°$); dyad **3** e) as cast ($\Delta^T = 19$ nm, $\Delta^{Ph} = 60°$) and f) after SVA ($\Delta^T = 21$ nm, $\Delta^{Ph} = 115°$). Scale bars set at 200 nm.

reveal phase contrast[13] and only homogeneous flat surfaces were identified.[25]

2.7.3. Grazing-Incidence Wide-Angle X-Ray Scattering Measurement

The thin-film organization of dyads 1–3 was investigated by GIWAXS. For the measurements, the films were solution cast at analogous conditions, as for the solar cell devices on substrates covered by PEDOT:PSS. For films before SVA, diffuse reflections in the GIWAXS patterns indicate a high disorder for all three dyads (Figure S41, Supporting Information). After 30 s of SVA, molecular ordering is enhanced as evident by the appearance of characteristic distinct reflections. Nevertheless, the overall order is still relatively moderate after SVA. Among the series, the molecular order of dyad 1 is slightly higher in comparison with 2 and 3, as evident from the clear π-stacking peak at 1.75 Å^{-1} (**Figure 13**a). In agreement with the SAED data (vide supra), a π-stacking distance of 0.36 nm is found for all three dyads, suggesting only a minor effect of the spacer length between the oligomer core and PC$_{61}$BM on the molecular spacing within the layers. The isotropic distribution of the π-stacking reflection implies some randomly arranged domains on the substrate. The small-angle reflection at around 0.41–0.44 Å^{-1} corresponds to a layer organization of the molecules (Figure 13b, S41, SI). The interlayer distance shifts from 1.42 nm for 1 to 1.53 nm for 3 with increasing spacer length. The out-of-plane position of this reflection is characteristic of a preferential edge-on arrangement of the oligomer cores on the surface, despite the coexistence of randomly oriented domains as previously mentioned. The PC$_{61}$BM phase gives rise to the typical broad and intensive reflection observed also for binary heterojunctions with polymers[34,35] and small molecules[36] as donors as well as for single covalently linked molecular D–A systems[25,37] and corresponds to a d-spacing from 0.48 nm for 1 to 0.45 nm for 3. The slightly tighter packing of the substituted PC$_{61}$BM might arise from a larger flexibility of the longer spacer in 3. The structural analysis confirms that SVA enhances the molecular ordering in the films of all three dyads 1–3, leading to the improvement in solar cell efficiency and charge carrier transport in OFETs. The GIWAXS results also reveal only slight variations in the organization between the dyads, as already observed for the device performances.

2.7.4. Model of the Molecular Arrangement of Best-Performing Dyad 1 in Thin Films

To better understand the molecular arrangement of dyads 1–3 in thin films, theoretical density functional theory calculations (CAMB3LYP and MO62x exchange correlation functionals and 6-31G++(d,p) basis) on the best-performing dyad 1 as an individual molecule and on small ordered aggregates were carried out. In a first step, different conformations of the isolated molecule were calculated. As expected, due to the flexibility of the spacer between the oligothiophene donor moiety and the PC$_{61}$BM pendant group, a rather smooth multipotential landscape of conformations was found. In one of the analyzed conformations, the PC$_{61}$BM unit and the alkyl chains lie coplanar to the oligothiophene: calculations on small aggregates of this conformer, however, showed no stabilization, most probably because of the poor layer-forming capability, which might be due to the different volumes of the donor and acceptor moieties, impeding intermolecular interactions perpendicular to the molecular plane. A conformation of dyad 1, in which the alkyl chains remain coplanar to the oligothiophene moiety and PC$_{61}$BM pending out of the molecular plane, was much more promising with respect to the aggregation behavior (**Figure 14**, middle). This noncoplanar D–A dyad 1 was analyzed regarding the capability of aggregation by calculating the energy gained by approaching two molecules in different parallel and antiparallel orientations in all three crystallographic axes and taking TEM, ESI, and GIWAXS findings into account. As a result, a molecular model of the best periodic arrangement of dyad 1 in a film is shown in Figure 14. The donor parts of the molecules arrange in a lamellar structure, in which C–H⋯N intermolecular interactions[38,39] and London dispersion forces between the alkyl chains[40] (red and blue dashed circles, Figure 14, left) stabilize the monolayer. PC$_{61}$BM units are bent down with respect to the yz-plane. The periodic distance between the π-systems is calculated to 1.5 nm. The monolayer formation, driven by the interdigitation of hexyl chains attached to the oligothiophene backbone, is common for all dyads as the corresponding model for the longer D–A dyad 3. Because of the out-of-plane bending of the pendant spacer PC$_{61}$BM moiety, the distances between the donor parts in the model are similar for all three dyads, independent of spacer length (Figure S43, Supporting Information).
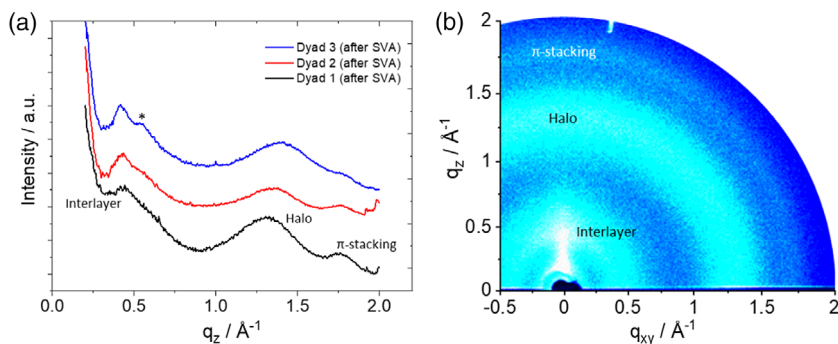

Figure 13. a) Out-of-plane profiles of dyads 1–3 after SVA (asterisk indicates PEDOT:PSS peak from Figure S41, Supporting Information) and b) GIWAXS pattern of 1 after SVA.
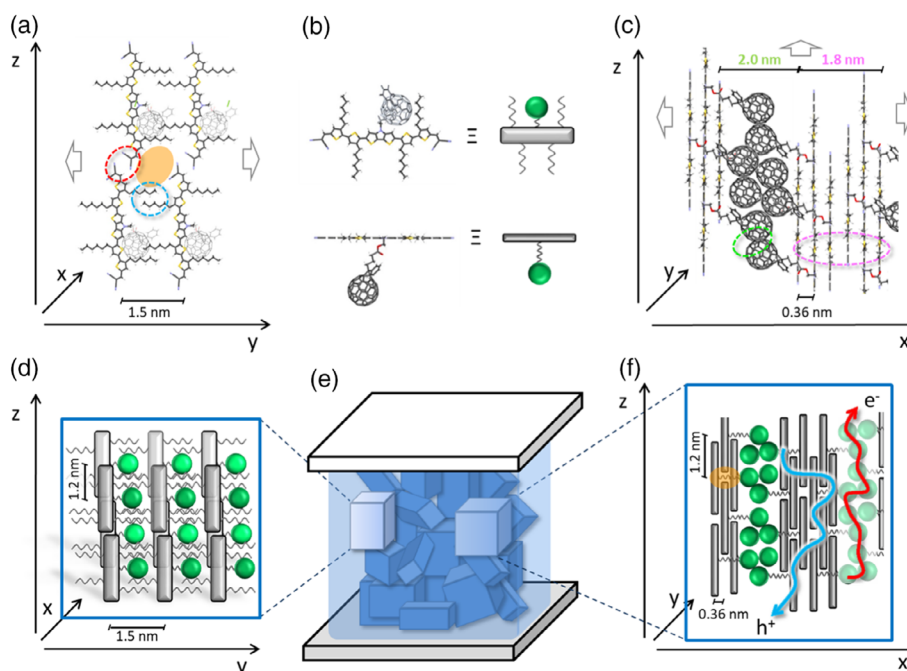
Figure 14. a) Molecular order of dyad **1** in the yz-plane: C–H$\cdots$N intermolecular interactions of the dicyanovinylene end groups and alkyl chain interdigitation are highlighted (red and blue dashed circles). A less-densely packed area between molecules is labeled by an orange oval (left). b) Molecular geometry of dyad **1** in the front and side view and corresponding sketch. b) Molecular order of dyad **1** in the xz-plane: intermolecular π interactions between the donor parts (magenta-dashed circle) and between PCBM units (green-dashed circle) are highlighted. White arrows indicate growth directions (right). d) Sketch of the supramolecular arrangement of dyad **1**: two layers of offset molecules (labeled with light and dark colors) ordered in the yz-plane: distances between the π-systems are 1.5 nm and offsets in z-direction are 1.2 nm. e) Sketch of a film of dyad **1** in between two electrodes (grey and white plates) composed of crystallites embedded in an amorphous phase (light blue). f) Sketch of the supramolecular arrangement in the xz-plane: channels of the $\pi-\pi$-stacking donor (grey) and interacting PC$_{61}$BM acceptor (green) subunits are shown. Postulated paths for the transport of holes and electrons are highlighted with blue and red arrows, respectively. A less-densely packed area between molecules labeled by a plain orange circle. Axes are taken arbitrarily.

The calculated distance between the π-systems in yz-direction for all dyads **1–3** is in very good agreement with the values (1.42–1.53 nm) obtained from GIWAXS and SAED measurements. Normal to the molecular plane (x-direction), π−stacking of the donor units at a distance of 0.36 nm is found (Figure 14c), which is also in agreement with GIWAXS results. The interacting oligothiophene backbones in this direction are offset by 1.2 nm, keeping an overlap of 60% of the π-system (Figure 14d,f). This overlap should be crucial for the excellent charge carrier (hole) transport (vide infra). The PC$_{61}$BM units of the molecules in the second layer percolate through the first layer at the molecular ends close to the DCV groups, which are less densely packed (orange circle in Figure 14a,f). The π-stacking in this direction is then limited in our model to few layers of molecules due to the pending PC$_{61}$BMs (Figure 14c) which is again in agreement with the GIWAXS results. Despite the limited persistence of π-stacking in the x-direction, an antiparallel arrangement of bundles of lamellae ensures the alternating crystalline growth of oligothiophene and PC$_{61}$BM components (Figure 14c). This molecular arrangement generates thin channels of the separated donor and acceptor phases with widths of 1.8 and 2.0 nm, respectively, growing in the y- and z-direction (Figure 14c,f). To complement our model, a sketch showing the active film of the dyad containing anisotropically oriented crystallites embedded in a phase of amorphously oriented molecules and sandwiched in between two electrodes is shown in Figure 14e. The reduced

anisotropic size of the phases in the calculated crystallites correlates with the lack of domain visualization from ESI data and with the assumption that domain sizes should be well below the 5 nm resolution threshold. Concerning the acceptor phases, it is fair to say that although the PC$_{61}$BM units in the model seem to pack closely, still about 30% free space is available in the channels. This observation explains the absence of a clear peak for the crystalline arrangement of PC$_{61}$BMs in the GIWAXS and SAED data and correlates with the moderate electron transport results. Finally, a path for electron transport in the acceptor channels and a pathway for holes in the donor channels, both indispensable for successful photovoltaic devices, seem to be warranted by our model (blue and red arrows in Figure 14c).

3. Conclusion

Novel D–A dyads **1–3** have been prepared in multistep syntheses in good overall yields. The synthetic design includes an oligothiophene donor and fullerene PC$_{61}$BM acceptor unit covalently linked by flexible alkyl ester spacers with variable lengths. The influence of this structural variation in the dyads on molecular and solid-state properties was investigated. The photovoltaic performance of dyads **1–3** as the sole photoactive component in SMOSCs gave the sequence $3 > 2 > 1$ for as-cast films with 2.90% PCE for **3** with the longest spacer as the best result.

The ranking was reversed for films after post-treatment by SVA and SMOSCs containing dyad 1 with the shortest spacer yielding a high PCE of 4.26% for oligomeric systems including high intrinsic stability under light and thermal stress. The photovoltaic results are uniquely tightly correlated with ambipolar transport measurements of the dyads **1**–**3**. As the photovoltaic and transport properties were strongly influenced and improved by SVA, investigations on the surface and bulk morphology revealed a relatively low crystallinity and order of molecular packing. The predominant ordering of the oligomeric donor π-system is indicated and the fullerenes mainly stay unaffected and their homoaggregation is already present in the pristine state. Calculations on the molecular and supramolecular level of the dyads yielded a model for the arrangement of dyads with alternating lamellae forming interfaces and channels of donor and acceptor units.

Our molecular design, i.e., the covalent linkage and precise distance of the donor and acceptor results in strongly confined lamellae of nanoscopic dimensions in the range of 2 nm, allowing for crucial phase separation as an important key in well-performing and highly stable SMOSCs. The overall elaborated qualitative structure–property–device performance relationships for our D–A dyads **1**–**3** will be helpful to support the rational design of improved materials and reach SMOSCs with higher efficiencies.

Supporting Information

Supporting Information is available from the Wiley Online Library or from the author.

Acknowledgements

Conflict of Interest

The authors declare no conflict of interest.

[1] S. Knorr, A. Grupp, M. Mehring, G. Grube, F. Effenberger, *J. Chem. Phys.* **1999**, *110*, 3502.

[2] M. Natali, S. Campagne, F. Scandola, *Chem. Soc. Rev.* **2014**, *43*, 4005.

[3] A. Zieleniewska, F. Lodemeyer, A. Roth, D. M. Guldi, *Chem. Soc. Rev.* **2018**, *47*, 702.

[4] L. Liu, P. Eisenbrandt, T. Roland, M. Polkehn, P.-O. Schwartz, K. Bruchlos, B. Omienciensky, S. Ludwigs, N. Leclerc, E. Zaborova, J. Léonard, S. Méry, I. Burghardt, S. Haacke, *Phys. Chem. Chem. Phys.* **2016**, *18*, 18536.

[5] L. F. Dössel, V. Kamm, I. A. Howard, F. Laquai, W. Pisula, X. Feng, C. Li, M. Takase, T. Kudernac, S. De Feyter, K. Müllen, *J. Am. Chem. Soc.* **2012**, *134*, 5876.

[6] F. Zhang, M. Svensson, M. R. Andersson, M. Maggini, S. Bucella, E. Menna, O. Inganas, *Adv. Mater.* **2001**, *13*, 1871.

[7] E. Peeters, P. A. van Hal, J. Knol, C. J. Brabec, N. S. Sariciftci, J. C. Hummelen, R. A. J. Janssen, *J. Phys. Chem. B* **2000**, *104*, 10174.

[8] F. Lin, K. Jiang, W. Kaminsky, Z. Zhu, A. K. Yen, *J. Am. Chem. Soc.* **2020**, *142*, 15246.

[9] J. Roncali, *Adv. Energy Mater.* **2011**, *1*, 147.

[10] J. Roncali, I. Grosu, *Adv. Sci.* **2019**, *6*, 1801026.

[11] X. Jiang, J. Yang, S. Karuthedath, J. Li, W. Lai, C. Li, C. Xiao, L. Ye, Z. Ma, Z. Tang, F. Laquai, W. Li, *Angew. Chem., Int. Ed.* **2020**, https://doi.org/10.1002/anie.202009272.

[12] Y. He, T. Heumüller, W. Lai, G. Feng, A. Classen, X. Du, C. Liu, W. Li, N. Li, C. Brabec, *Adv. Energy Mater.* **2019**, *9*, 1900409.

[13] W. Wang, R. Sun, J. Guo, J. Guo, J. Min, *Angew. Chem., Int. Ed.* **2019**, *58*, 14556.

[14] S. Lucas, T. Leydecker, P. Samorí, E. Mena-Osteritz, P. Bäuerle, *Chem. Commun.* **2019**, *55*, 14202.

[15] C. Wessendorf, A. Perez-Rodriguez, J. Hanisch, A. Arndt, I. Ata, G. Schulz, A. Quintilla, P. Bäuerle, U. Lemmer, P. Wochner, E. Ahlswede, E. Barrena, *J. Mater. Chem. A* **2016**, *4*, 2471.

[16] S. Dkhil, M. Pfannmöller, I. Ata, D. Duché, M. Gaceur, T. Koganezawa, N. Yoshimoto, J. Simon, L. Escoubas, C. Videlot-Ackermann, O. Margeat, S. Bals, P. Bäuerle, J. Ackermann, *J. Mater. Chem. A* **2017**, *5*, 1005.

[17] I. Ata, S. Dkhil, M. Pfannmöller, S. Bals, D. Duché, J. Simon, T. Koganezawa, N. Yoshomoto, C. Videlot-Ackermann, O. Margeat, J. Ackermann, P. Bäuerle, *Org. Chem. Front.* **2017**, *4*, 1561.

[18] F. Li, S. Wang, Y. Zhang, J. L. Lutkenhaus, *Chem. Mater.* **2018**, *30*, 5169.

[19] C. Wessendorf, G. Schulz, A. Mishra, P. Kar, I. Ata, M. Weidelehner, M. Urdanpilleta, J. Hanisch, E. Mena-Osteritz, M. Linden, E. Ahlswede, P. Bäuerle, *Adv. Energy Mater.* **2014**, *4*, 1400266.

[20] A. Mishra, P. Bäuerle, *Angew. Chem., Int. Ed.* **2012**, *51*, 2020.

[21] S. Izawa, K. Hashimoto, K. Tajima, *Synth. Met.* **2012**, *162*, 2201.

[22] T. Nishizawa, K. Tajima, K. Hashimoto, *Chem. Commun.* **2009**, 2469.

[23] J. Min, X. C. Jiao, I. Ata, A. Osvet, T. Ameri, P. Bäuerle, H. Ade, C. J. Brabec, *Adv. Energy Mater.* **2016**, *6*, 1502579.

[24] J. Min, X. C. Jiao, V. Sgobba, B. Kan, T. Heumüller, S. Rechberger, E. Spieker, D. Guldi, X. Wan, Y. Chen, H. Ade, C. J. Brabec, *Nano Energy Mater.* **2016**, *28*, 241.

[25] T. L. Nguyen, T. H. Lee, B. Gautam, S. Y. Parl, K. Gundogdu, J. Y. Kim, H. Y. Woo, *Adv. Funct. Mater.* **2017**, *27*, 1702474.

[26] T. Heumüller, W. R. Mateker, A. Distler, U. F. Fritze, R. Cheacharoen, W. H. Nguyen, M. Bielem, M. Salvador, M. von Delius, H.-J. Egelhaaf, M. D. McGehee, C. J. Brabec, *Energy Environ. Sci.* **2016**, *9*, 247.

[27] T. Leydecker, M. A. Squillaci, F. Liscio, E. Orgiu, P. Samorì, *Chem. Mater.* **2019**, *31*, 6491.

[28] M. Pfannmöller, W. Kowalsky, R. R. Schröder, *Energy Environ. Sci.* **2013**, *6*, 2871.

[29] M. Pfannmöller, H. Flügge, G. Benner, I. Wacker, C. Sommer, M. Hanselmann, S. Schmale, H. Schmidt, F. A. Hamprecht, T. Rabe, W. Kowalsky, R. R. Schröder, *Nano Lett.* **2011**, *11*, 3099.

[30] W. Lai, C. Li, J. Zhang, F. Yang, F. J. M. Colberts, B. Guo, Q. M. Wang, M. Li, A. Zhang, R. A. J. Janssen, M. Zhang, W. Li, *Chem. Mater.* **2017**, *29*, 7073.

[31] X. Yang, J. K. J. van Duren, M. T. Rispens, J. C. Hummelen, R. A. J. Janssen, M. A. J. Michels, J. Loos, *Adv. Mater.* **2004**, *16*, 802.

[32] M. Casalegno, S. Zanardi, F. Frigerio, R. Po, C. Carbonera, G. Marra, T. Nicolini, G. Raos, S. V. Meille, *Chem. Commun.* **2013**, *49*, 4525.

[33] D. Popovic, I. Ata, J. Krantz, S. Lucas, M. Linden, E. Mena-Osteritz, P. Bäuerle, *J. Mater. Chem. C* **2017**, *5*, 9920.

[34] F. Machui, S. Rathgeber, N. Li, T. America, C. J. Brabec, *J. Mater. Chem.* **2012**, *22*, 15570.

[35] N. Li, J. D. Perea, T. Kassar, M. Richter, T. Heumueller, G. J. Matt, Y. Hou, N. S. Güldal, H. Chen, S. Chen, S. Langner, M. Berlinghof, T. Unruh, C. J. Brabec, *Nat. Commun.* **2017**, *8*, 14541.

[36] S. D. Oosterhout, V. Savikhin, J. Zhang, Y. Zhang, M. A. Burgers, S. R. Marder, G. C. Bazan, M. F. Toney, *Chem. Mater.* **2017**, *29*, 3062.

[37] Z. Luo, F. Wu, T. Zhang, X. Zeng, Y. Xiao, T. Liu, C. Zhong, X. Lu, L. Zhu, S. Yang, C. Yang, *Adv. Mater.* **2018**, *30*, 1706124.

[38] R. Fitzner, E. Mena-Osteritz, A. Mishra, G. Schulz, E. Reinold, M. Weil, C. Körner, H. Ziehlke, C. Elschner, K. Leo, M. Riede, M. Pfeiffer, C. Uhrich, P. Bäuerle, *J. Am. Chem. Soc.* **2012**, *134*, 11064.

[39] R. Fitzner, C. Elschner, M. Weil, C. Uhrich, C. Körner, M. Riede, K. Leo, M. Pfeiffer, E. Reinold, E. Mena-Osteritz, P. Bäuerle, *Adv. Mater.* **2012**, *24*, 675.

[40] R. Azumi, G. Götz, T. Debaerdemaeker, P. Bäuerle, *Chem. Eur. J.* **2000**, *6*, 735.